Applied Catalysis A: General 488 (2014) 248–255

Contents lists available at ScienceDirect

Applied Catalysis A: General

journal homepage: www.elsevier.com/locate/apcata

Effects of multivariate linker substitution, metal binding, and reactor conditions on the catalytic activity of a Pd-functionalized MOF for olefin hydrogenation

Trenton Otto[a,b], Nanette N. Jarenwattananon[a], Stefan Glöggler[a], Jonathan W. Brown[a], Arek Melkonian[a], Yavuz N. Ertas[c], Louis-S. Bouchard[a,c,d,*]

[a] University of California at Los Angeles, Department of Chemistry and Biochemistry, 607 Charles E Young Drive East, Young Hall 3048B, Los Angeles, CA 90095-1059, USA
[b] University of California at Los Angeles, Chemical and Biomolecular Engineering Department, 420 Westwood Plaza, Box 951592, 5531 Boelter Hall, Los Angeles, CA 90095-1592, USA
[c] University of California at Los Angeles, Department of Bioengineering, 420 Westwood Plaza, Room 5121, Engineering V, P.O. Box 951600, Los Angeles, CA 90095-1600, USA
[d] California NanoSystems Institute, 570 Westwood Plaza, Building 114, Mail Code 722710, Los Angeles, CA 90095-8352, USA

ARTICLE INFO

Article history:
Received 29 July 2014
Received in revised form
27 September 2014
Accepted 5 October 2014
Available online 14 October 2014

Keywords:
Metal organic framework
Multivariate principle
Heterogeneous catalysis
Palladium
Propylene

ABSTRACT

We investigated the performance of zinc-based metal-organic framework (MOF) catalysts that were post-synthetically modified with the homogeneous palladium catalyst $Pd(CH_3CN)_2Cl_2$ for the hydrogenation of propylene in a packed-bed, tubular microreactor. The catalytic conversion and apparent reaction kinetics were analyzed across a range of metal loadings, reactant flow rates, feed concentrations, and reactor temperatures. The catalyst's deactivation in the presence of a common palladium catalyst poison, carbon monoxide, was also examined. The catalytic conversion was optimal at moderate metal loadings, stoichiometric excess of hydrogen, and relatively mild temperatures. The activity depended strongly on reactant feed composition but showed no dependence on total flow rate, indicating a diffusion-limited process. To investigate the effects of intra-particle diffusion limitations, internal diffusion coefficients for propylene in the MOF catalysts were measured with pulsed field gradient nuclear magnetic resonance (PFG NMR) and were incorporated into the kinetics analysis. Using these coefficients to compute effectiveness factors for heterogeneous catalytic reactions, diffusion-limited artifacts were accounted for to obtain intrinsic rate constants and activation energies from apparent kinetics data. The average intrinsic activation energy was found to be 51(6) kJ/mol. The MOF catalyst was also found to be reversible under carbon monoxide poisoning, suggesting a weak binding mechanism.

1. Introduction

MOFs are reticular assemblies composed of metal cluster vertices coordinated to connecting edges consisting of organic functional groups [1,2]. Two of the most common methods to synthesize MOFs for catalysis include preparation of MOFs with catalytically active open metal sites, and postsynthetic modification [3]. In the former case, coordinatively unsaturated (open) metal nodes can act as active sites for gas adsorption [1,4,5] as well as catalysis in liquid phase reactions and more infrequently in gas phase reactions [6]. During postsynthetic modification, functional groups or catalytically active centers are covalently bonded or embedded into the MOF framework via chemical reaction [3,7]. This method offers versatility in preparing a single MOF matrix as a support for vastly different reactions because functional groups on the organic linker can be bonded to a wide variety of active materials. For instance, the IRMOF-3 structure alone has been postsynthetically modified with a vanadium acetylacetonate complex for the oxidation of cyclohexene [8], zinc hydroxide species for aromatic alkylation [9], and an Au(III) complex for butadiene hydrogenation [10]. Yet another dimension of variability can be added by utilizing multiple linkers in the synthesis, which creates the opportunity to bind broad classes of active species to the framework, and alter

* Corresponding author at: University of California at Los Angeles, Department of Chemistry and Biochemistry, 607 Charles E Young Drive East, Young Hall 3048B, Los Angeles, CA 90095-1059, USA. Tel.: +1 310 825 1764.
E-mail addresses: bouchard@chem.ucla.edu, louis.bouchard@gmail.com (L.-S. Bouchard).

http://dx.doi.org/10.1016/j.apcata.2014.10.012
0926-860X/

the MOF pore size and topology [11,12]. These factors mean that MOFs have many potential applications in heterogeneous catalysis [13]. With the highest surface area to volume ratio known to date among crystalline compounds, MOFs may be designed to possess a high density of catalytically active sites [14].

At this time, studies aimed at optimizing MOF-catalyzed heterogeneous reactions in packed-bed reactors are scarce. In this article we study an IRMOF-3 structure covalently bonded to the $Pd(CH_3CN)_2Cl_2$ palladium complex as the active material. Previously reported Pd-MOFs with a sodalite-type structure have been shown to be competitive in gas adsorption [15] as well as alcohol oxidation, Suzuki C–C coupling, and olefin hydrogenation reactions [16]. The introduction of palladium into the regular pore system of a MOF was shown to impart selective entry of reactant molecules into the framework, which results from constricted access to the MOF interior and the blockage of diffusion of large molecules due to steric hindrance [16]. This demonstrates how the active site environment can be altered when palladium catalysts are immobilized onto a MOF framework.

We examined the continuous-flow hydrogenation of propylene in a packed-bed reactor (PBR) using five isoreticular MOF (IRMOF-3) catalysts synthesized with different organic link ratios. Metal centers for catalysis were added by using two linker groups that differ from each other by the absence or presence of an amino group which can be reacted further to attach a Pd catalyst to the framework. The ratio of 2-amino-benzene-1,4-dicarboxylic acid (amino-BDC) to benzene-1,4-dicarboxylic acid (BDC) used in the synthesis of the MOF (prior to final metalation with Pd catalyst) enables tuning of the framework [17–20]. Five distinct MOF samples were synthesized by treating $Zn_4O(BDC\text{-}NH_2)_n(BDC)_{(3-n)}$ (where $n = 3$, 2.4, 1.8, 1.2, and 0.6) with salicylic aldehyde to yield an imine derivative, and metalated with Pd to create a palladium functionalized framework. The value of n is used to indicate the ratio of amino-BDC to BDC linker groups used in the synthesis. For example, $Zn_4O(BDC\text{-}NH_2)_{1.8}(BDC)_{1.2}$-Pd is used to indicate a metalated IRMOF synthesized with amino-BDC making up 60% of the added linker groups and BDC as the remaining 40%. Reported procedures exhibit more details regarding the synthesis of IRMOF structures with BDC and amino-BDC functional groups [17]. Through inductively coupled plasma mass spectrometry (ICP-MS) and Brunauer–Emmett–Teller (BET) analysis, we have shown that MOF samples with higher amino-BDC content exhibit more palladium loading to the framework, but at the cost of lower specific surface area. We also examined the catalytic activity, reactant diffusion, reaction kinetics, and carbon monoxide poisoning of $Zn_4O(BDC\text{-}NH_2)_n(BDC)_{(3-n)}$-Pd for $n = 3$, 2.4, 1.8, 1.2, and 0.6 and found that the intermediate system, $Zn_4O(BDC\text{-}NH_2)_{1.8}(BDC)_{1.2}$-Pd, demonstrated the most optimal properties for catalytic conversion.

2. Experimental

2.1. Catalyst synthesis

All $Zn_4O(BDC\text{-}NH_2)_n(BDC)_{(3-n)}$-Pd samples were prepared in similar fashion to the following example for $Zn_4O(BDC\text{-}NH_2)_{0.6}(BDC)_{2.4}$, except for varying starting ratios of amino-BDC and BDC [17,18]. Utilizing a two-step postmodification reaction, imine condensation followed by metalation, all frameworks were metalated using identical synthetic conditions. To synthesize $Zn_4O(BDC\text{-}NH_2)_{0.6}(BDC)_{2.4}$-Pd, amino-BDC (63 mg, 0.34 mmol), BDC (108 mg, 0.65 mmol), and zinc nitrate hexahydrate (890 mg, 3 mmol) were added to *N*,*N*-dimethylformamide (DMF) (50 mL) and sonicated until the components were fully dissolved. The static solution was heated at 85 °C for 24 h to form single crystals. The crystals were collected and washed with DMF for three days, then exchanged into toluene and reacted with salicylic aldehyde (1 mL, 7.12 mmol) at 50 °C for 5 days. The sample was exchanged with dry toluene to remove unreacted salicylic aldehyde, yielding $Zn_4O(BDC\text{-}NH_2)_{0.6}(BDC)_{2.4}$-imine. Toluene exchanged $Zn_4O(BDC\text{-}NH_2)_{0.6}(BDC)_{2.4}$-imine (≈100) was solvent exchanged with CH_2Cl_2 over a 2-h period. $PdCl_2(CH_3CN)_2$ (50 mg, 0.19 mmol) was dissolved in CH_2Cl_2 (40 mL) to which the $Zn_4O(BDC\text{-}NH_2)_{0.6}(BDC)_{2.4}$-imine was added in minimum solvent. The reaction was allowed to stand at room temperature for two days, and then washed with CH_2Cl_2 over a three-day period. The solvents were removed from the pores of the framework by dynamic vacuum (at 30 mTorr) for 12 h at 85 °C to yield $Zn_4O(BDC\text{-}NH_2)_{0.6}(BDC)_{2.4}$-Pd.

2.2. Catalyst characterization

BET analysis, powder X-ray diffraction (PXRD), scanning electron microscopy (SEM), ICP-MS, and digestion NMR were used to characterize the five MOF samples.

2.2.1. N_2 adsorption and BET analysis

N_2 adsorption isotherms for each MOF sample were measured for use in BET analysis. Following activation of the MOF samples, isotherms for each were measured using nitrogen at 77 K. Low-pressure gas adsorption experiments (below 760 Torr) were performed on a Quantachrome NOVA 4200e automatic volumetric gas adsorption analyzer. Ultra-high purity grade N_2 (99.999% purity) and a liquid nitrogen bath (77 K) were used for N_2 isotherm measurements. For measurement of the surface areas, the BET method was applied using the adsorption branches of the N_2 isotherms assuming a N_2 cross-sectional area of 16.2 $Å^2$/molecule.

2.2.2. Powder X-ray diffraction

PXRD data for each sample were collected using a Bruker D8-Discover θ–θ diffractometer in reflectance Bragg–Brentano geometry employing Ni filtered Cu Kα line focused radiation at 1600 W (40 kV, 40 mA) power and equipped with a Vantec Line detector. Radiation was focused using parallel focusing Gobel mirrors. The system was also outfitted with an anti-scattering shield that prevents incident diffuse radiation from hitting the detector in order to mitigate the normally large background signal at $2\theta < 3$. Samples were mounted on glass slides by dropping powders from a wide-blade spatula and then leveling the sample with a razor blade.

2.2.3. Inductively coupled plasma mass spectroscopy

ICP-MS measurements were conducted on each of the five MOF samples with a Thermo-Finnegan Element XR spectrometer (Thermo Fisher Scientific Analytical Technologies, Massachusetts, USA) to measure their Pd content.

2.2.4. Scanning electron microscopy

SEM images for each of the five MOF samples were collected using a Jeol JSM-7500F field emission scanning electron microscope. The resulting images were used to estimate the mean particle sizes for each of the five MOF samples examined, using a sample size of 40 particles.

2.2.5. Digestion NMR

Digestion NMR was employed to measure the ratios of BDC and amino-BDC linker groups that bind to the framework in the final metalated MOF complexes. The MOF samples were treated with a deuterated dimethyl sulfoxide (DMSO-d_6) and DCl mixture to dissolve and hydrolyze the BDC and amino-BDC linker groups, and ^1H spectra on the resulting liquid determined the ratio of the two linkers in the synthesized catalysts. NMR spectroscopy was performed

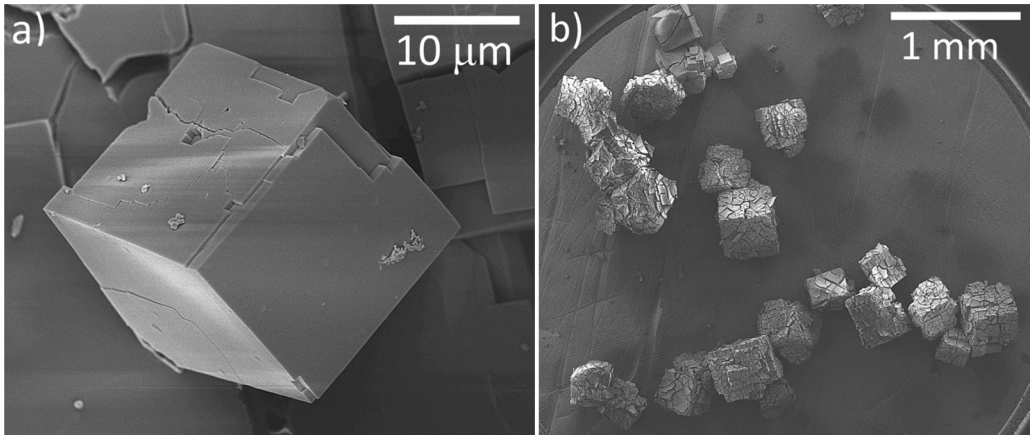

Fig. 1. SEM images of $Zn_4O(BDC\text{-}NH_2)_{0.6}(BDC)_{2.4}$-Pd at two different length scales.

using a Bruker Avance 600 MHz superconducting magnet (Bruker Corporation, Massachusetts, USA) running TopSpin 2.1 software

2.3. Catalytic reaction testing

2.3.1. Packed bed reactor assembly

The tubular packed bed reactor consisted of a 5.08-cm long and 0.318-cm internal diameter copper pipe with affixed tube fittings (Swagelok Ltd., Ohio, USA). 30.0 mg of MOF or palladium on carbon catalyst were packed into the tubular reactor for each trial discussed, and 0.138 cm frits (Applied Porous Technologies, Connecticut, USA; average pore size 2 μm) were used to plug each end of the packed bed and keep the bed in place. The catalyst bed itself was 1 cm long for each trial, leading to a packing density of 378 mg/cm^3. Prior to the introduction of reactants, the catalyst bed was activated under nitrogen gas flow for 15 min. Reactant gases flowing into the bed first pass through a preheating copper coil to ensure that the gases were at the proper temperature before entering the reactor. The reactor and preheating coil assembly were placed in a Lindberg Blue M tube oven (Thermo Fisher Scientific Analytical Technologies, Massachusetts, USA) that provided external heating for temperature modulation. We verified that isothermal conditions with the surrounding oven prevailed throughout this reactor by inserting thermocouples at various locations. A diagram of the reactor setup can be found in Fig. S2 (Appendix).

2.3.2. Flow assembly

Hydrogen gas and propylene gas were flowed through the system for all experiments. The inlet pressure was fixed at 103.4 kPa for each trial. The pressure drop across the reactor was small (2% of the inlet pressure or less). For poisoning experiments, carbon monoxide gas was also flowed through the reactor to induce the poisoning. Mass flow controllers (Cole-Parmer, Illinois, USA) were used to regulate the gas flows. The separate gas flows were adjoined with a T junction for mixing prior to entry into the reactor. All gases were purchased of industrial purity from AirGas.

2.3.3. Gas composition analysis

NMR spectroscopy was performed using a Bruker Avance 600 MHz superconducting magnet (Bruker Corporation, Massachusetts, USA) running TopSpin 2.1 software to collect propylene and propane gas spectra. A 5 mm triple inverse broadband probe tuned to ^{1}H resonance was used to collect proton spectra. The relative intensities of the methyl ($-CH_3$) resonances were analyzed in Topspin via peak integration to determine the catalytic conversion of propylene to propane. Effluent gases from the reactor were fed directly into the 5 mm NMR probe's radiofrequency region to allow continuous collection of spectral data. NMR spectra at selected points in time followed by off-line analysis in MATLAB (The MathWorks, Natick, MA) allowed computation of catalytic conversion through peak integration. A sample NMR spectrum and details behind the computation of the conversion can be found in the Appendix.

Gas chromatography–mass spectrometry (GC/MS) analysis was also performed on selected samples to validate NMR readings and confirm complete selectivity for propane. No side products were detectable with either method.

2.3.4. Temperature and reactant flow optimization

The temperature optimization experiments were performed on $Zn_4O(BDC\text{-}NH_2)_n(BDC)_{(3-n)}$-Pd for $n = 3$, 2.4, 1.8, 1.2, 0.6. The conversion of each catalyst was measured over the temperature range 303–483 K in 10 K intervals under 50 sccm H_2 flow and 5 sccm propylene flow. A 15 min time period was allowed to elapse between each temperature measurement to promote the establishment of a steady state. Furthermore, the reaction was allowed to run for 30 min at 303 K prior to the collection of the first data point to allow for any transient start-up effects to be mitigated. Data from these trials were used to calculate rate constants and activation energies for each catalyst. The reactant composition and total flow rate were optimized for $Zn_4O(BDC\text{-}NH_2)_{1.2}(BDC)_{1.8}$-Pd. The hydrogen:propylene ratio was varied from 1–14 and the total reactor feed was varied from 15 sccm to 90 sccm at 373 K.

2.4. Reactant diffusion measurements with pulsed field gradient NMR

PFG NMR signals are made sensitive to the mean-square-displacement ($r^2(\Delta)$) of molecules during a diffusion time, Δ, by attenuating the signal using a pair of opposite-polarity magnetic-field gradient pulses separated by Δ. This technique has been used to probe diffusion mechanisms within the MOF crystallite [21,22]. We have performed PFG NMR measurements on a Varian 9.4 Tesla VNMRS microimaging system using a standard PFG stimulated echo (PFG STE) pulse sequence with variable gradient strength whose amplitude we denote as g, and gradient pulse length as δ [23]. Propylene gas at atmospheric pressure, room temperature (298 K), and in the absence of hydrogen was passed through a packed bed filled with $Zn_4O(BDC\text{-}NH_2)_{1.8}(BDC)_{1.2}$-Pd catalyst powder positioned in the sensitive region of the detector coil. The magnetic field gradient pulses were applied in a direction perpendicular to the bulk flow velocity to minimize the impact of flow on measurements of the diffusion coefficient. The flow rate was kept fixed at

Table 1
Summary of quantitative characterization data for the $Zn_4O(BDC\text{-}NH_2)_n(BDC)_{(3-n)}$-Pd samples[a].

n	Wt % Pd	BET surface srea (m^2/g)	% Imine linkers	Average particle size (mm)
0.6	0.0012	1650	28	0.5
1.2	0.0026	1640	38	0.3
1.8	0.0043	610	68	0.3
2.4	0.0059	430	87	0.6
3	0.0063	210	100	0.5

[a] Errors in Wt% Pd are ~10%, errors in % Imine Linkers are 1%, particle size errors are ~15%, BET surface areas may vary by up to $\pm 10\ m^2/g$.

50 sccm for each trial, and space velocities were identical to those used in the packed bed reactor experiments. Diffusion measurements were performed under flow to better mimic the pressure and hydrodynamic conditions in our operating reactor. The timing diagram of the PFG STE sequence is shown in Fig. S18 (Appendix). The parameters were: $\tau = 500\ \mu s$, $\delta = 100\ \mu s$ (with gradient ramp time, 100 μs), $10\ ms \leq \Delta \leq 300\ ms$ and gradient amplitudes g from 0 G/cm to 50 G/cm.

2.5. Catalyst poisoning with carbon monoxide

For each poisoning trial, a fresh catalyst bed was prepared by packing MOF powder in a tubular reactor, and reactant gas flow rates identical to those discussed in Section 2.3 were used. The external temperature of the reactor and preheating coil were maintained at either 373 K or 423 K for two sets of experiments. First, a reaction was run without any carbon monoxide (CO) mixed with the reactants. This reaction was run for 30 min to achieve steady state catalytic conversion. After 30 min, the catalytic conversion (based on product composition) was measured via NMR spectroscopy to obtain the percent conversion prior to the addition of CO. After this measurement, carbon monoxide was added to the inlet stream of the reactor, and the composition of the emerging stream was measured every second for 370 s. Immediately following the period of catalyst poisoning, the CO feed to the reactor was shut off and the recovery in activity was again monitored over time via NMR spectroscopy. This procedure was repeated for CO flow rates of 0.5 sccm, 1 sccm, and 2 sccm on different samples of MOF. Analogous poisoning experiments were also performed on 30 mg of palladium on carbon (PdC) samples in an identical reactor to compare trends in the poisoning between the MOF and PdC catalysts.

3. Results and discussion

3.1. Characterization

SEM images of the five MOF samples of $Zn_4O(BDC\text{-}NH_2)_n(BDC)_{(3-n)}$-Pd showed cubic crystals with average sizes of approximately 0.5 mm, 0.6 mm, 0.3 mm, 0.3 mm, and 0.5 mm for $n = 3$, 2.4, 1.8, 1.2, and 0.6 respectively. Fig. 1 shows sample SEM images of $Zn_4O(BDC\text{-}NH_2)_{0.6}(BDC)_{2.4}$-Pd at two different scales. Smooth and rigid structures like the one shown in Fig. 1(a) can be seen by zooming in on the surfaces of the MOF particles shown in Fig. 1(b). The crystallites shown in Fig. 1(b) exhibit surface cracking, but maintain approximately cubic shapes. Images for the remaining four samples can be found in Fig. S11–S12 (Appendix). Additional images were also collected in order to achieve a sample size of 40 particles, though not all images are shown here.

ICP-MS and BET analysis were used to quantify the palladium content in weight percent and specific surface areas of the MOFs, respectively. Results of the ICP-MS and BET measurements are shown in Table 1. Samples with lower levels of amino-BDC (and thus lower levels of metal loading) were found to exhibit greater specific surface area. This result implies that increased binding of the active metal species to the framework may cause pore blockage and reduce the access of gas molecules to the interior of the MOF crystallites. Indeed, it appears that the MOF pores are blocked by the addition of both salicyldehyde and Pd into the framework, which could have the effect of making the pore volume slightly smaller. Similar effects have been seen in other MOFs grafted with Pd through imine condensation [19]. N_2 adsorption isotherms can be found in Fig. S5 (Appendix).

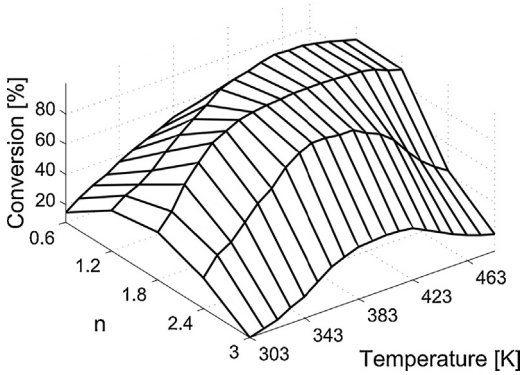

Fig. 2. Catalytic conversion as a function of the relative amount of amino-BDC used in the MOF synthesis and reactor temperature at 103.4 kPa. Feed flow rates: 5 ccm propene at STP, 50 ccm hydrogen at STP, weight hour space velocity (WHSV) is $28\ h^{-1}$.

Figures S13–S17 (Appendix) show the ^1H spectra collected for each of the digested MOF samples. The ratio of linkers measured in the metalated MOFs (e.g. percent imine linkers) was slightly different from the ratio of linker groups used in the synthesis, which we denote by the subscript n. This discrepancy is due to the fact that the ratio of linkers used in the synthetic procedure does not always match perfectly with the linker ratio in the end product [17]. Table 1 shows the percent yield of imine formation for each of the five MOF samples considered.

The crystallinity of each of the five MOF samples was verified by PXRD. Figures S6–S7 (Appendix) present PXRD patterns for each MOF sample following activation. PXRD patterns were also collected following heat treatment to assess losses in crystallinity as a result of thermal damage. Structural changes in the MOF samples as a result of heating are discussed in Section 3.2.

3.2. Catalytic performance with respect to temperature, metal loading, and reactant feed

The performance of the MOF catalysts was examined and optimized with respect to four parameters: reaction temperature, ratio of amino-BDC to BDC, reactant feed ratio, and flow rate. Results of the temperature optimization for the MOFs are shown in Fig. 2. $Zn_4O(BDC\text{-}NH_2)_{1.8}(BDC)_{1.2}$-Pd was found to exhibit the greatest product conversion. Brunauer–Emmett–Teller analysis (see Table 1) revealed that the MOFs prepared with higher amino-BDC content [namely, the $Zn_4O(BDC\text{-}NH_2)_{2.4}(BDC)_{0.6}$-Pd and $Zn_4O(BDC\text{-}NH_2)_3$-Pd cases] also have lower specific surface. Lower surface-to-volume ratios likely lead to reduced adsorption of reactants on the crystallite framework. This may explain why $Zn_4O(BDC\text{-}NH_2)_{2.4}(BDC)_{0.6}$-Pd and $Zn_4O(BDC\text{-}NH_2)_3$-Pd resulted in lower conversion than $Zn_4O(BDC\text{-}NH_2)_{1.8}(BDC)_{1.2}$-Pd. The $Zn_4O(BDC\text{-}NH_2)_{1.8}(BDC)_{1.2}$-Pd strikes a more optimal balance between active metal content and surface area, resulting in its being the most effective MOF catalyst in our experiments.

This series of MOFs achieves maximum catalytic activity at ≈393 K, and beyond which, they experience nearly constant

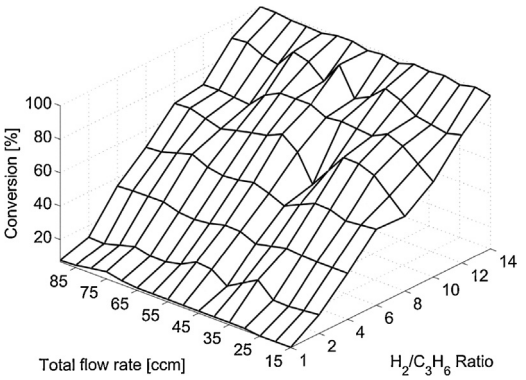

Fig. 3. Dependence of catalytic conversion on reactant composition and flow rate for $Zn_4O(BDC\text{-}NH_2)_{1.2}(BDC)_{1.8}$-Pd at 373 K and 103.4 kPa. Catalyst mass is 30 mg with packing density 378 mg/cm^3.

activity followed by a decline in activity. Heating to temperatures above 423 K results in permanent deactivation of the MOF. The catalytic conversion is plotted in Fig. 2.

Thermal gravimetric analysis (TGA) and PXRD analysis on $Zn_4O(BDC\text{-}NH_2)_{1.8}(BDC)_{1.2}$-Pd (see Figs. S6–S8, Appendix) both suggest that structural damage occurs in the MOF at temperatures above ≈423 K, correlating with the loss of activity at elevated temperatures shown in Fig. 2. TGA indicates that loss of mass in the catalyst occurs near 393 K. PXRD spectra were taken on each of the five MOF samples before and after 5 h of heat treatment under inert gas flow at 423 K. The results demonstrate significant structural damage in the case of the heated samples (see Figs. S6 and S7, Appendix for PXRD patterns). Thermal damage [24] in these MOFs occurs at temperatures lower than industrial catalysts such as zeolites [25]. To determine the extent of deactivation over the range 303–393 K, we continuously reacted each of the five samples for five hours at 303 K, and also for 5 h at 393 K. Results of these time on stream (TOS) experiments indicated minimal decline in activity. Data and details on each of the ten TOS experiments performed can be found in the Appendix.

In Fig. 3, we isothermally varied reactant feed ratio and flow rate. Catalytic conversion increases linearly with hydrogen content whereas varying the volumetric flow rate has negligible effect, even over a wide range of flow rate values. Providing a stoichiometric excess of hydrogen in the feed increases propane yield, but the catalytic conversion has a weak dependence on overall flow rate.

Increasing the reactant flow rate would be expected to improve the rate of reaction on a per-mass of catalyst basis in reactors whose reaction rate is limited by inter-phase (external) mass transport [26–28]. However, this is not necessarily the case for systems whose performance is limited by intra-particle diffusion rather than reaction kinetics or transport between the catalyst surface and the bulk fluid phase. Applying the Weisz-Prater criterion and the Mears criterion (see Section S3, Appendix) [27–29], the MOF catalysts are shown to operate in the internal diffusion-limited regime. The relatively large particle sizes used in this study (Table 1) are the probable causes for the intra-particle limitations evidenced by the results of Weisz-Prater analysis. Reducing the crystal size would likely help to mitigate intra-particle diffusion limitations, though no methods for systematically synthesizing crystals of a particular size have yet been developed for these MOF species. We were unable to maintain the crystallinity of our frameworks when attempting to reduce particle size through ball grinding. However, for the purpose of determining the reaction kinetics, transport and particle size effects are accounted for through the use of effectiveness factor relations summarized by Madon and Boudart [27].

3.3. MOF-catalyzed reaction kinetics

The kinetics of the reaction were analyzed in terms of the apparent rate constant (k) assuming an Arrhenius rate law:

$$k(T) = A(T)e^{-E_a/RT} \tag{1}$$

where E_a is the activation energy, R is the ideal gas constant, T is temperature, and $A(T)$ is the pre-exponential factor. The latter encompasses a combination of rate and equilibrium constants for the reaction. Its value may depend on temperature, type of catalyst, and packing used in the reaction. We derived apparent values of k using the data of Fig. 2 by relating it to the catalytic conversion via the axial dispersion model for packed bed reactors:

$$v_x\frac{dc}{dx} - D\frac{d^2C}{dx^2} - \dot{r} = 0 \tag{2}$$

where c is the concentration of limiting reactant (propylene), v_x is the flow velocity, and D is propylene's axial dispersion coefficient [27]. The observed rate of generation term $\dot{r}$ was assumed to follow elementary kinetics, taking the form: $\dot{r} = -kc[H_2]$ where k is the apparent rate constant of Eq. (1). The assumption that the reaction rate is first order with respect to hydrogen is a strong one, as a wide variety of palladium-catalyzed hydrogenation studies have found first order dependence with respect to hydrogen [30], and indeed palladium catalyzed hydrogenation is generally first order with respect to hydrogen [31].

In this form of the rate law, the rate constant k incorporates the effects of transport limitations by intra-particle diffusion. The intrinsic rate constant k_i can be related to the apparent rate constant k through the use of an internal effectiveness factor η, such that $\dot{r} = -k_i\eta c[H_2]$, where η is dependent on the transport limitations involved and is a function of physical constants (including particle size and internal diffusion coefficients) and the reactant concentrations [27]. In systems where both external and internal transport effects are significant, an overall rather than an internal effectiveness factor would be used in the intrinsic rate expression. However, the results of Weisz-Prater and Mears analysis indicate that external transport resistance is minuscule, allowing the use of η. Furthermore, minimal external transport resistance means that bulk concentrations rather than surface concentrations can be used in the rate law [25].

By applying criteria that quantifies the importance of axial dispersion effects in the reactor concentration profile [26], we determined that the second order derivative term in Eq. (2) can be neglected (see Section S2, Appendix). With the added assumption that the hydrogen concentration exhibits minimal variation across the catalyst bed, Eq. (2) can be simplified and integrated immediately. Experimentally, the hydrogen concentration varied by an average of only 5.6% across all trials, which is due to the large excess of hydrogen used in the feed. Applying these simplifications results in an expression relating the apparent rate constant to the inlet and outlet propylene concentrations:

$$k = -\frac{v_x}{[H_2]L}\ln\left(\frac{c_L}{c_0}\right) \tag{3}$$

where c_L is the outlet concentration, c_0 is the inlet concentration, and L is the length of the catalyst bed (1.0 cm). Apparent rate constants derived in this manner can be simply related to intrinsic rate constants using a procedure described by Madon and Boudart, which requires information on the particle dimensions described in Section 3.1, and also measurements of internal diffusion coefficients for propylene [27], discussed in Section 3.4.

A collection of rate constants corresponding to different temperatures were calculated, allowing the intrinsic and apparent activation energies of the reaction to be derived from a fit to the Arrhenius equation. Fig. 4(a) shows the intrinsic reaction rate

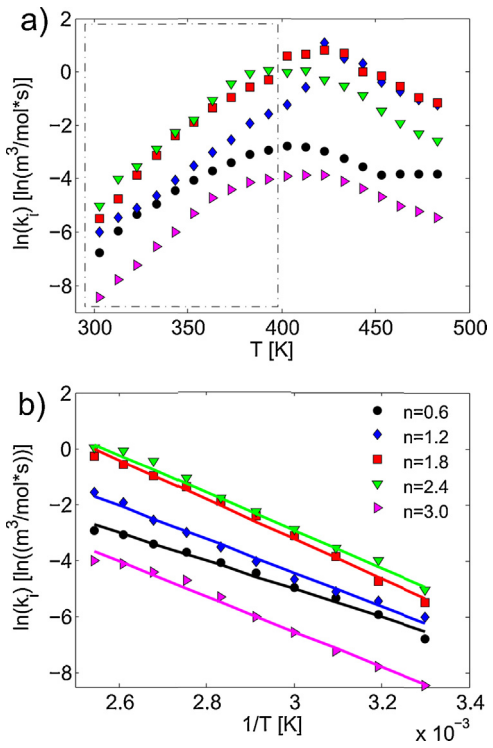

Fig. 4. (a) Temperature dependence of the intrinsic kinetic rate constant k_i (T) for each MOF. (b) Arrhenius plot of the rate constants over the reduced temperature range 303–393 K, as indicated by the box in (a).

constants for all of the five MOF samples over the entire temperature range examined, and Fig. 4(b) displays a linearized Arrhenius plot over the temperature range 303–393 K. Section S2 (Appendix) also contains apparent kinetics data on all of the MOFs examined.

Similar to the conversion data in Fig. 2, the apparent and intrinsic rate constants increase in an Arrhenius fashion over the temperature range 303–393 K. Beginning at 393 K, the increase in rate constant with activation energy begins to stagnate and eventually drops. This drop correlates with the onset of thermal damage to the MOF, as measured by PXRD and TGA (described in Section 3.2 and Section S4, Appendix). Structural damage may affect gas adsorption or limit the number of available active sites, leading to a reduced rate constant. Over the temperature range 303–393 K, where the structural integrity of the MOF remains intact, the relationship between reaction temperature and the rate constant is fit well by the Arrhenius equation, as can be seen in Fig. 4(b). The fact that the rate constants derived from the model presented in Eq. (3) are fit well to the Arrhenius equation validates that this reaction is approximately first order with respect to propylene over the range of compositions examined: as using an incorrect reaction order in the model would result in poor fits to the Arrhenius equation. The intrinsic activation energy and Arrhenius pre-exponential factor were extracted from Fig. 4 for each MOF, the results of which are collected in Table 2.

Table 2
Intrinsic activation energies, Arrhenius prefactors, and maximum rate constants for $Zn_4O(BDC\text{-}NH_2)_n(BDC)_{(3-n)}$.

n	E_a (kJ/mol) (Apparent)	E_a (kJ/mol) (Intrinsic)	$\log_{10}(A)$ [$\log_{10}$(m^3/mol s)]	k_i (m^3/mol s)
0.6	23(2)	41(4)	4(1)	0.062(4)
1.2	27(2)	49(4)	6(1)	3.0(2)
1.8	32(3)	58(5)	8(1)	2.3(2)
2.4	30(3)	56(5)	7(1)	0.91(6)
3	28(3)	52(5)	5(1)	0.021(1)

The activation energies for each MOF sample listed in Table 2 are similar and typically within the random error of each other, suggesting that the activation energy does not vary appreciably with metal loading. The dominant factor in our reaction's yield is the Arrhenius pre-exponential factor, which for $Zn_4O(BDC\text{-}NH_2)_{1.8}(BDC)_{1.2}$-Pd has the largest A value by far (Table 2 reports logarithms of A). The Arrhenius pre-exponential factor may consist of a combination of rate and equilibrium constants for a reaction, and when transport artifacts are accounted for (as is the case here), is mainly influenced by catalyst active site geometry. An important difference between the apparent and intrinsic kinetic parameters is the magnitude of activation energies, as the intrinsic E_a values are nearly double the apparent values. This is consistent with a diffusion-limited process [26,27]. In practice, this result implies that methods to remove internal diffusion limitations will impart stronger temperature dependence to the catalytic conversion. Physically, the tradeoff between specific surface and amino-BDC content of $Zn_4O(BDC\text{-}NH_2)_{1.8}(BDC)_{1.2}$-Pd makes it the most catalytically active overall, which is also reflected in the maximum intrinsic rate constant observed for intermediate metal loadings.

3.4. Reactant diffusion in MOF crystallites

Determining the timescale of reactant diffusion is important in identifying the catalyst with the optimal structure for this reaction and the impact of reactant transport. Estimates of the diffusion timescale require measurements of the reactant intra-crystalline self-diffusion coefficients. We measured the gas diffusion using PFG NMR [23] by probing resonances from the limiting reactant, propylene. In this experiment, the measured signal intensity $S(b)$ is related to the parameter $b = (2\gamma g\delta)^2(\Delta - \delta/3)$ via $S(b) = S_0\exp(-bD)$, which enables extraction of propene's diffusion coefficient, D, from the slope in a plot of ($\ln S(b)/S_0$) versus b [23]. Values of the gradient amplitude g, diffusion time Δ, and pulse length δ are listed in Section 2.4; γ is the proton gyromagnetic ratio. The single and stretched exponential did not provide good models for the experimental data. Instead a sum of two exponentials worked best:

$$S(b) = S_1 e^{-bD_1} + S_2 e^{-bD_2} \quad (4)$$

where D_1 and D_2 are diffusion coefficients of components 1 and 2, with amplitudes S_1 and S_2, respectively. This model suggests compartmentalization of the diffusing molecules into two separate fractions. It has been used to model a variety of multi-component diffusion mechanisms in other MOF materials [21], including the self-diffusion of hydrocarbons in IRMOF-1 [22], which is topologically similar to our catalyst.

A plot of ($\ln(S(b)/S_0)$) vs. b, enabling extraction of the self-diffusion coefficients, is shown in Fig. 5. This plot consists of two straight lines, each of which with a distinct slope, corresponding to two distinct environments of translational diffusion. The larger of the two components (D_1), is attributed to bulk propylene flow through the inter-crystalline space, and the smaller of the two (D_2) represents the intra-crystalline (inside the MOF crystallite) component. Since D_1 results from molecular motion in the inter-crystalline space, it is influenced by free-gas diffusion; however, it is not identical to the free gas diffusion coefficient for propylene due to the aforementioned bulk propylene flow between and around the MOF crystallites.

Intra-crystalline diffusion coefficients were measured for each of the five MOF samples examined. The average intra-crystalline diffusion coefficient for $Zn_4O(BDC\text{-}NH_2)_{1.8}(BDC)_{1.2}$-Pd, which is shown in Fig. 5, was $8(1)\cdot10^{-7}$ m^2/s. Diffusion coefficients for $n = 3$, 2.4, 1.2, and 0.6 were $1.0(2)\cdot10^{-6}$, $7(2)\cdot10^{-7}$, $8(2)\cdot10^{-7}$, and $7(2)\cdot10^{-7}$ m^2/s respectively (see Section S5, Appendix for raw data).

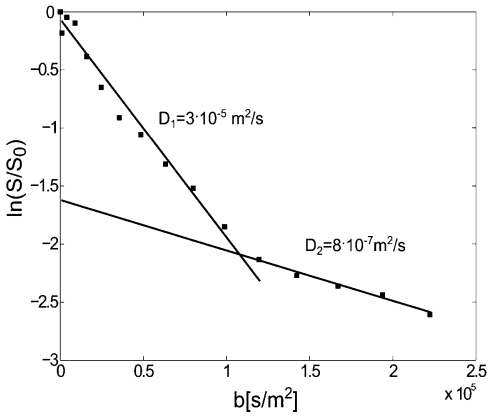

Fig. 5. PFG STE signal attenuation: logarithmic decay of the NMR signal intensity ($\ln S(b)/S_0$) with the parameter b in $Zn_4O(BDC\text{-}NH_2)_{1.8}(BDC)_{1.2}$-Pd. D_1 is due to bulk gas flow through the reactor. D_2 is due to self-diffusion inside the crystallite (intracrystalline diffusion).

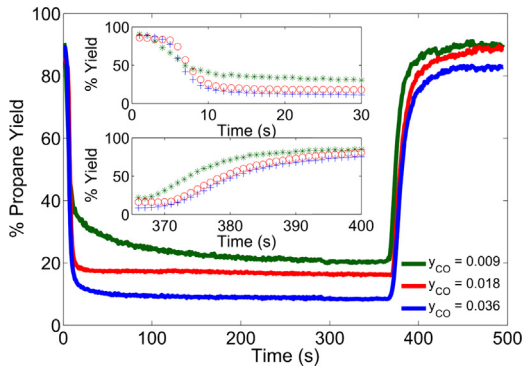

Fig. 6. Carbon monoxide deactivation and recovery of $Zn_4O(BDC\text{-}NH_2)_{1.8}(BDC)_{1.2}$-Pd at 373 K with 5 ccm propylene and 50 ccm hydrogen (WHSV = 28 h^{-1}). Carbon monoxide is introduced to the feed at time t = 0 s and shut off at time t = 370 s. Colored lines correspond to different mole fractions (y_{CO}) of CO in the feed. The two subplots (insets) in the figure zoom in on the poisoning curve during initial deactivation (upper subplot) and recovery (lower subplot).

Reducing or increasing the propylene residence time by a factor of two resulted in identical D_2 values in test trials, validating that D_2 is nearly independent of bulk flow conditions and describes internal diffusion. Each of these coefficients is within random error of each other, indicating that the differences in intra-crystalline diffusion coefficients arising from different linker ratios agree within experimental uncertainty. We suspect that Pd and salicyldehyde act to block the MOF pore entrances, making it more difficult for reactants to diffuse into or out of the crystallite as metalation increases. However, the effect of pore volume reduction has been seen to be small in some Pd-loaded MOF species [32], so it is possible that once in the crystal, the open pore size is similar, giving rise to similar intracrystalline diffusion coefficients.

These diffusion coefficients were used to compute effectiveness factor terms, η, in the transport-corrected rate law, $\dot{r}$, shown in Eq. (2). The diffusion coefficients also vary with temperature, and this dependence was assumed to scale as $D_2 \propto \sqrt{T}$ (the case of Knudsen diffusion). The typically reported small pore diameter of 11.2 Å for MOF-5 structures [33] also indicates transport dominated by Knudsen diffusion.

3.5. Catalyst deactivation by carbon monoxide poisoning

Because catalysts may lose activity over time due to poisoning by contaminants [30], reversibility with respect to poisoning is desirable. CO is a common poison for hydrocarbon reactions, including hydrogenations, and for palladium in particular [34–37]. Though CO is a catalyst poison, it is common for CO to be intentionally added to the feed stream in palladium-catalyzed hydrogenation reactions, as doing so has been shown to improve the selectivity of desired hydrogenations (for example, the hydrogenation of ethyne in the presence of olefins) when multiple unsaturated hydrocarbon species and competing reactions are present [30,38–40]. As a result, the investigation of CO poisoning is of great interest. This is especially true of the $Zn_4O(BDC\text{-}NH_2)_n(BDC)_{(3-n)}$-Pd species examined in this work, as palladium MOFs have been shown to impart selective hydrogenation on the basis of the structure of the supporting framework [16]. This effect combined with CO poisoning could result in enhanced selectivity in hydrogenation reactions.

Poisoning trials were performed whereby the catalytic conversion of the MOF was measured, first as the catalyst was poisoned, and again as it recovered its activity following cessation of exposure. Analogous experiments were also performed on PdC for comparison (see Section S6, Appendix). In these trials, readouts were made at every second and a model was fit to extract the decay in catalytic activity. The decay in activity exhibited by the PdC was best modeled with a single exponential. In contrast, the modeling of decay in the MOF activity required a double exponential. Section S6 (Appendix) contains raw data and further details regarding the poisoning trials. The double exponential is often indicative of two distinct physical mechanisms controlling the rate of decay, whereas a single exponential implies a single-mechanism process. This discrepancy between the MOF and PdC deactivation data is likely due to their distinct structural differences: MOFs are crystalline with ordered pores while PdC is an amorphous, disordered material. Indeed, studies on gas adsorption into MOFs indicate that a biexponential trend in sorbate uptake commonly occurs [41,42]. Because reaction in the MOF is a diffusion-limited process, the biexponential decay in activity mirrors the uptake of carbon monoxide over time, whereby adsorption results from entry of the CO through the pore apertures of the framework, followed by diffusion of the CO once inside the pore.

Fig. 6 shows the CO deactivation and recovery of $Zn_4O(BDC\text{-}NH_2)_{1.8}(BDC)_{1.2}$-Pd at 373 K at three different CO concentrations. After 370 s of exposure, the flow of CO was stopped. Following this cessation to exposure, the MOFs exhibited excellent reversibility with respect to carbon monoxide poisoning, as evidenced by recovery of the full activity in all cases. Higher concentrations of CO result in a more dramatic drop in activity as well as a more delayed recovery following cessation of exposure. The reversibility of the poisoning process in our MOFs is indicative of a physisorption mechanism, which is the adsorption process also seen in other MOF materials [43]. Even under continuous exposure to CO, the MOFs retain a degree of catalytic activity in the steady state. The steady state is reached following ≈300 s of exposure. This is a result of the equilibrium that is established between adsorption and desorption of the CO from poisoning sites. MOFs with higher catalytic activity [e.g. $Zn_4O(BDC\text{-}NH_2)_{1.2}(BDC)_{1.8}$-Pd and $Zn_4O(BDC\text{-}NH_2)_{1.8}(BDC)_{1.2}$-Pd] retain greater conversion under continuous exposure, suggesting a higher concentration of accessible active sites. Increasing the temperature of the poisoning experiments both increased the residual activity under constant poisoning and reduced the carbon monoxide desorption time following cessation of exposure, as is also observed with other transition metal catalysts [35].

4. Conclusions

We examined the effects of amino-BDC content, reactant flow rate and composition, and reaction temperature on the catalytic performance of a new palladium MOF catalyst in the

hydrogenation of propylene. We also determined the average intrinsic activation energy associated with the reaction, and investigated mechanisms of deactivation for the MOFs by CO poisoning and thermal degradation. Finally, we determined the self-diffusion coefficients of reactants in the MOF to better understand the role of intra-crystalline diffusion on the catalytic conversion. MOFs with intermediate levels of amino-BDC content were shown to exhibit the greatest activity, likely due to their optimal combination of specific surface area and metal loading. Total flow rate had little effect on conversion over the range of flow rates examined, though stoichiometric excesses of hydrogen improved propylene conversion in an approximately linear fashion. The MOFs performed optimally near 393 K, with average activation energy of 51(6) kJ/mol over the range 303–393 K. The MOFs exhibited excellent reversibility to CO poisoning, with deactivation controlled by a two-step mechanism characterized by two rate constants. It was shown by PXRD and time on stream experiments that catalyst deactivation occurs at temperatures above 423 K due to thermally induced structural damage. Measurements of the self-diffusion coefficient of propylene inside the MOF reactor yielded a diffusion coefficient of $8(2)\cdot10^{-7}$ m^2/s within each of the MOF crystallites. The apparent reaction kinetics were limited by intra-particle diffusion, which likely results from the high specific surface and narrow pores of MOFs through which reactants must diffuse to reach catalytically active metal centers. Thus, we conclude that optimization of MOF catalysts with respect to yield is important due to the competing effects of metalation and pore blocking. But also since pore blocking plays an important role in determining the yield, it may also play a role in the selectivity of the catalyst. Studies are underway in our laboratory to study the effects of metal loading on selectivity.

Acknowledgments

The work was partially funded by a Beckman Young Investigator Award, a Dreyfus New Faculty Award, and a NSF grant (CHE-1153159). We thank Hiroyasu Furukawa for performing BET measurements.

Appendix A. Supplementary data

Supplementary material related to this article can be found, in the online version, at http://dx.doi.org/10.1016/j.apcata.2014.10.012.

References

[1] D.K. Britt, H. Furukawa, B. Wang, T.G. Glover, O.M. Yaghi, Proc. Natl. Acad. Sci. U. S. A. 106 (2009) 20637–20640.
[2] N. Stock, S. Biswas, Chem. Rev. 112 (2012) 933–969.
[3] A. Corma, H. García, F.X. Llabrési Xamena, Chem. Rev. 110 (2010) 4606–4655.
[4] J.R. Li, Y. Ma, M.C. McCarthy, J. Sculley, J. Yu, H.K. Jeong, P.B. Balbuena, H.C. Zhou, Coord. Chem. Rev. 255 (2011) 1791–1823.
[5] M. Dincă, J.R. Long, Angew. Chem. Int. Ed. 47 (2008) 6766–6779.
[6] A.N. Mlinar, B.K. Keitz, D. Gygi, E.D. Bloch, J.R. Long, A.T. Bell, ACS Catal. 4 (2014) 717–721.
[7] P. Valvekens, F. Vermoortele, D. De Vos, Catal. Sci. Technol. 3 (2013) 1435–1445.
[8] M.J. Ingleson, J.P. Barrio, J.B. Guilbaud, Y.Z. Khimyak, M.J. Rosseinsky, Chem. Commun. 23 (2008) 2680–2682.
[9] U. Ravon, M.E. Domine, C. Gaudillere, A. Desmartin-Chomel, D. Farrusseng, New J. Chem. 32 (2008) 937–940.
[10] X. Zhang, F.X. Llabrés i Xamena, A. Corma, J. Catal. 265 (2009) 155–160.
[11] M. Yoon, R. Srirambalaji, K. Kim, Chem. Rev. 112 (2012) 1196–1231.
[12] D. Farrusseng, S. Aguado, C. Pinel, Angew. Chem. Int. Ed. 48 (2009) 7502–7513.
[13] A. Dhakshinamoorthy, M. Alvaro, H. Garcia, Chem. Commun. 48 (2012) 11275–11288.
[14] F. Song, C. Wang, W.A. Lin, Chem. Commun. 47 (2011) 8256–8258.
[15] J.A.R. Navarro, E. Barea, J.M. Salas, N. Masciocchi, S. Galli, A. Sironi, C.O. Ania, J.B. Parra, Inorg. Chem. 45 (2006) 2397–2399.
[16] F.X. Llabres i Xamena, A. Abad, A. Corma, H. Garcia, J. Catal. 250 (2007) 294–298.
[17] H. Deng, C.J. Doonan, H. Furukawa, R.B. Ferreira, J. Towne, C.B. Knobler, B. Wang, O.M. Yaghi, Science 327 (2010) 846–850.
[18] M.J. Ingelson, J.P. Barrio, J.-B. Guilbaud, Y.Z. Khimyak, M.J. Rosseinsky, Chem. Commun. 23 (2008) 2680–2682.
[19] C.J. Doonan, W. Morris, H. Furukawa, O.M. Yaghi, J. Am. Chem. Soc. 131 (2009) 9492–9493.
[20] K.K. Tanabe, S.M. Cohen, Angew. Chem. Int. Ed. 48 (2009) 7424–7427.
[21] F. Stallmach, S. Gröger, V. Künzel, J. Kärger, O.M. Yaghi, M. Hesse, U. Müller, Angew. Chem. Int. Ed. 45 (2006) 2123–2126.
[22] D.C. Ford, D. Dubbeldam, R.Q. Snurr, V. Künzel, M. Wehring, F. Stallmach, J. Kärger, U. Müller, J. Phys. Chem. Lett. 3 (2012) 930–933.
[23] J.E. Tanner, J. Chem. Phys. 52 (1970) 2523–2527.
[24] L.H. Wee, S.R. Bajpe, N. Janssens, I. Hermans, K. Houthoofd, C.E.A. Kirschhock, J.A. Martens, Chem. Commun. 46 (2010) p8186.
[25] J. Lee, J.R. Farha, K.A. Scheidt, S.T. Nguyen, J.T. Hupp, Chem. Soc. Rev. 38 (2009) 1450–1459.
[26] H.S. Fogler, Elements of Chemical Reaction Engineering, third ed., Prentice Hall, Upper Saddle River, New Jersey, United States, 2006.
[27] R.J. Madon, M. Boudart, Ind. Eng. Chem. Fundam. 21 (1982) 438–447.
[28] C. Perego, S. Peratello, Catal. Today 52 (1999) 133–145.
[29] J.M.P.Q. Delgado, Heat Mass Transfer 42 (2006) 279–310.
[30] A.N.R. Bos, K.R. Westerterp, Chem. Eng. Process. 32 (1993) 1–7.
[31] Plc. Johnson Matthey, The Catalysis Technical Handbook, Johnson Matthey Plc, London, United Kingdom, 2005.
[32] Y. Huang, S. Gao, T. Liu, J. Lu, X. lin, H. Li, R. Cao, Chem. Plus. Chem. 77 (2012) 106–112.
[33] M. Eddaoudi, J. Jim, A. Rosi, D. Vodak, J. Watcher, O. O'Keeffe, O.M. Yaghi, Science 295 (2002) 469–472.
[34] M.G.T. Burrows, W.H. Stockmeyer, Proc. R. Soc. Lond. A 176 (1940) 474–484.
[35] M. Montano, K. Bratlie, M. Salmeron, G.A. Somorjai, J. Am. Chem. Soc. 126 (2006) 13229–13234.
[36] D.C. Tang, K.S. Hwang, M. Salmeron, G.A. Somorjai, J. Phys. Chem. B 108 (2004) 13300–13306.
[37] P. Chen, K.Y. Kung, Y.Y. Shen, G.A. Somorjai, Surf. Sci. 494 (2001) 289–297.
[38] G.C. Battiston, L. Dalloro, G.R. Tauszik, Appl. Catal. 2 (1982) 1.
[39] V.A. Men'shchikov, Y.G. Fal'kovich, M.E. Aerov, Kinet. Cutal. 16 (1975) 13355–21338.
[40] W.T. McGown, C. Kemball, D. Whan, J. Catal. 51 (1978) 173–184.
[41] B. Chen, X. Zhao, A. Putkham, K. Hong, E.B. Lobkovsky, E.J. Hurtado, A.J. Fletcher, K.M. Thomas, J. Am. Chem. Soc. 126 (2004) 9750–9759.
[42] A.J. Fletcher, E.J. Cussen, D. Bradshaw, M.J. Rosseinsky, K.M. Thomas, J. Am. Chem. Soc. 126 (2004) 9750–9759.
[43] J.L.C. Roswell, A.R. Millward, K.S. Park, O.M. Yaghi, J. Am. Chem. Soc. 126 (2004) 5666–5667.